Journal of Materials Chemistry A

Accepted Manuscript

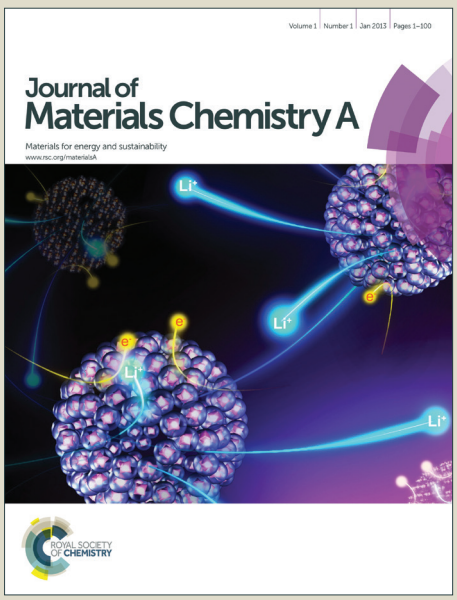

ROYAL SOCIETY OF CHEMISTRY

www.rsc.org/materialsA

Cite this: DOI: 10.1039/c0xx00000x

www.rsc.org/xxxxxx

ARTICLE TYPE

Computational and Experimental Analysis of $Ba_{0.95}La_{0.05}FeO_{3-\delta}$ as a Cathode Material for Solid Oxide Fuel Cells

Chi Chen,[a] Dengjie Chen,[a] Yang Gao,[a] Zongping Shao [c,d] and Francesco Ciucci[a,b]*

Received (in XXX, XXX) Xth XXXXXXXXX 20XX, Accepted Xth XXXXXXXXX 20XX

DOI: 10.1039/b000000x

Solid oxide fuel cells (SOFCs) may play a crucial role in solving the energy crisis because they are clean and energy efficient. Finding suitable cathode materials for SOFCs is key to facilitating their widespread usage. Besides developing high performance materials, understanding the stability and intrinsic properties of a material is equally important. Herein, $Ba_{0.95}La_{0.05}FeO_{3-\delta}$ (BLF) is studied combining molecular simulations and experiments on single crystal thin films. Lattice dynamics simulations are applied to study the stabilization of barium orthoferrate $BaFeO_{3-\delta}$ upon doping with La^{3+}. Simulation results reveal the defect energy for substituting one Ba^{2+} with La^{3+} in the cubic phase to be lower than that in the monoclinic phase, contributing to its stabilization. Analogous results are also found by doping the Ba site with Sm^{3+}, Gd^{3+} and Y^{3+}. In addition, the simulation results suggest that the charge compensation mechanism upon doping is filling oxygen vacancies and La^{3+} tends to trap the mobile oxygen anions. In turn, as the doping level increases the oxygen anion diffusivity decreases, as is also supported by molecular dynamics simulations. In light of this conclusion, single crystal thin films of La^{3+} slightly doped $BaFeO_{3-\delta}$, BLF, are grown on yttria-stabilized zirconia substrates using pulsed laser deposition. The polarization resistance of the dense film is 0.07 Ωcm^2 at 700 °C and ambient atmosphere, which is comparable to the state-of-the-art Co-based materials.

Introduction

The increasing energy demands and environmental challenges require high energy efficiency, low emission and fuel-versatile energy conversion devices. Solid oxide fuel cells (SOFCs) are among the most promising devices that match these requirements.[1-4] Typically, SOFCs operate at high temperature, around 1000 °C, which requires high thermal integrity in the system design and special materials that can be stable at high temperature. Lowering the temperature to the intermediate range, from 500 to 750 °C, not only reduces the cost of meeting the thermal requirement standard but also allows the use of less expensive materials, particularly for the interconnects and balance-of-plant components.[5] In addition, the reduced operating temperature slows down materials degradation, greatly extending the cell's durability. Therefore, lowering the operating temperature is crucial in the research of SOFCs. However, due to the smaller ionic conductivity and slower reaction rate, the reduced temperature causes greater electrolyte Ohmic resistance and polarization resistance. Generally, the Ohmic resistance results from the ionic transport and is an extensive quantity related to the transport distance. The polarization resistance, however, is correlated to the catalytic property of the material. While the Ohmic resistance could be effectively reduced by decreasing the thickness of the electrolyte,[6] reducing the polarization resistance becomes the central problem. This is most critical at the cathode side where the oxygen reduction reaction (ORR) takes place. It is generally believed that ORR kinetics is the bottleneck of low-temperature SOFCs.[7] Therefore, developing an effective cathode material is crucial to facilitate the broad application of SOFCs.

Among all the cathode materials, perovskite-type materials have shown promising performance.[3, 8] The perovskite materials, with a general form of $ABO_{3-\delta}$, have the advantage that their material properties, such as oxygen conductivity, electronic conductivity and the surface oxygen exchange rate, may be tailored by doping the A or B sites. In an attempt to synthesize and select proper perovskite materials for the cathode, several factors need to be considered. First, the materials need to possess high performance properties, such as high mixed-ionic-electronic conductivity and surface oxygen exchange rate. Second, the material must be phase stable, chemically stable and thermally stable. Third, the material price should be reasonably low. Various perovskite materials for SOFC cathode have been proposed, but most suffer from tradeoffs between stability, performance and cost. Several perovskite-type materials commonly exist, namely manganites, cobaltites and ferrites.[9] Sr-doped $LaMnO_3$ (LSM) is one type of manganite material that is most commonly used in industry. Even though it is quite chemically stable with respect to the commonly used yttria-stabilized zirconia (YSZ) electrolyte and, with adjustment, its thermal expansion can be compatible with YSZ, it behaves like a pure electronic conductor due to the low oxygen vacancy concentration.[10] Co-based perovskite materials, such as

$La_{1-x}Sr_xCo_{1-y}Fe_yO_{3-\delta}$,[11-15] $Sm_{0.5}Sr_{0.5}CoO_{3-\delta}$,[16-18] $Pr_{0.4}Sr_{0.6}Co_{0.2}Fe_{0.7}Nb_{0.1}O_{3-\delta}$[19] and $Ba_{0.5}Sr_{0.5}Co_{0.8}Fe_{0.2}O_{3-\delta}$ (BSCF),[8, 20, 21] exhibit high electrocatalytical and conductive properties due to the high concentration of disordered oxygen vacancies and the presence of Co, which is reflected by the small area-specific resistance. However, the price is typically high due to the presence of the rare metal Co and the phase stability of the material may be an issue. For example, the renowned BSCF is characterized by extraordinary properties and has been used in oxygen permeation membranes[22-24] and in SOFC cathodes.[8, 20, 21] However, at intermediate temperature and ambient oxygen content, it is observed that the high performance cubic phase BSCF becomes unstable and gradually changes to the low performance hexagonal phase.[25-27] Another class of cathode materials for SOFCs is based on Fe, a cheap and abundant element. These include, for example, $Ba_{0.5}Sr_{0.5}Zn_{0.2}Fe_{0.8}O_{3-\delta}$,[28, 29] $BaCe_xFe_{1-x}O_{3-\delta}$,[30] $Sr_2Fe_{1.5}Mo_{0.5}O_{6-\delta}$[31, 32] and $Ba_{0.95}La_{0.05}FeO_{3-\delta}$ (BLF).[33-35] Despite the low price, Fe-based materials have shown promising performance, most notably the BLF. BLF was originally developed by slightly doping barium orthoferrate $BaFeO_{3-\delta}$ (BF) with La on the Ba site. Compared to $SrFeO_{3-\delta}$, the mother material BF has larger cations at the A site, which potentially increases the ionic conductivity.[36] By doping BF with La, it was observed that the previous mixed phases were stabilized to a single cubic perovskite phase. Interestingly, when BLF was used in oxygen permeation membranes, it exhibited the best oxygen permeation flux among other stoichiometric ratios.[33, 37] Efforts have also been made to apply this material towards cathodes for SOFCs,[34, 35] where high structural stability and high oxygen vacancy concentration were demonstrated. Most importantly, the electrocatalytical properties of BLF were shown to be comparable to the state-of-the-art cobaltites, making it a suitable cathode material for SOFCs.

Although several researchers have reported BLF in oxygen permeation membranes and SOFCs, some fundamental issues remain unsolved. First, the stabilization of BF to single cubic phase upon doping is not well understood. Previously it was explained by the Goldschmidt tolerance factor of the ABO_3 cubic perovskite,[34, 37] defined as,

$$t_G = (r_A + r_O)/(\sqrt{2}(r_B + r_O)) \qquad (1)$$

where r_A, r_B and r_O are ionic radii for A site cation, B site cation and oxygen anion respectively, which are usually taken from Shannon's table.[38] However, the tolerance factor can only be used to justify the stabilization results but it does not serve as a fundamental understanding of why the stabilization would occur. Second, it was observed in the oxygen permeation membrane experiments that increasing the doping level of La resulted in a decrease of the oxygen permeation flux, which was attributed to the decrease of oxygen vacancy concentration,[37] but the reason for the decrease of vacancy concentration was unclear. It is known that the vacancy concentration does not uniquely determine the oxygen permeation. Factors such as the activation energy for oxygen anion hopping could also greatly affect the oxygen movement inside the material. In order to address these two questions, atomistic simulations are employed. The results reveal that BLF is reasonably stable and has better oxygen transport properties than the doped BF with higher La content. Therefore, the experimental investigations were performed on BLF. Unlike previous investigations of BLF, which have been conducted primarily on geometrically ill-defined porous structures, the investigations were conducted on single crystal thin films. In the porous samples, factors such as porosity and tortuosity make the identification of the intrinsic material properties rather difficult. One study was conducted on geometrically well-defined dense films,[35] but the samples presented were polycrystalline, making it still difficult to decouple the material properties from the properties of defects such as the grain boundaries. Herein the single crystal thin films of BLF as SOFC cathodes were studied. This study of La^{3+} doped BF may also provide useful information for other BF-related materials.

Methodology and approach

Molecular simulation

Structural optimizations, defect energy calculations and molecular dynamics (MD) simulations were carried out using an empirical potential model. Computations from the electronic structure method using, for example, density functional theory, are attractive approaches since they provide more information about the electronic configuration that can be linked to many physical properties.[39-41] In the case for small doping, however, the supercell that is needed for reproducing the doping level is usually large, making the computation challenging. In addition, the electronic structure computation is typically performed at 0 K, which produces material properties that are different to those of high temperature situations. In this case, the empirical force-field potential model in a MD framework is a good choice for simulating the molecular behavior. Herein, we assume pairwise interactions between ions, which include long-range Coulombic interactions, short-range atomic repulsions and Van der Waals forces. The potential describing the pair interaction between two ions, indexed α and β, is of the following Buckingham form:

$$\Phi_{\alpha\beta} = \frac{Z_\alpha Z_\beta e^2}{4\pi\epsilon r_{\alpha\beta}} + A_{\alpha\beta}\exp(-\frac{r_{\alpha\beta}}{\rho_{\alpha\beta}}) - \frac{C_{\alpha\beta}}{r_{\alpha\beta}^6} \qquad (2)$$

where Z_α and Z_β are the charge numbers of the two interacting ions, e is the elementary charge, ϵ is the dielectric constant, $r_{\alpha\beta}$ is the separation distance between the two ions. The potential parameters, $A_{\alpha\beta}$, $\rho_{\alpha\beta}$ and $C_{\alpha\beta}$, are taken from previously published articles.[42-44] For specific parameter values, please see the supplementary information. The ions are treated using their formal charges,[45] e.g., oxygen with a -2 charge.

Structural optimization and defect energy calculations were performed within the quasi-harmonic approximation as implemented in the general utility lattice program (GULP).[46] During the optimization with a nonzero temperature, the Gibbs free energy, instead of the potential energy, was used as the objective functional. The defect calculations used the Mott-Littleton approach,[47, 48] where the inner region I radius was 12 Å and an outer region IIa radius was 30 Å. For the calculation convergence, the energy tolerance was set to 10^{-5} eV and the force tolerance is set to 10^{-3} eV/Å. In the GULP molecular model, the cubic phase is studied using two primitive cells (1×1×2) and the monoclinic phase is studied using one primitive unit cell, which consists of a total number of 126 atoms ($Ba_{28}Fe_{28}O_{70}$).

The oxygen diffusivity was computed by MD using the large-

scale atomic/molecular massively parallel simulator (LAMMPS).[49] For the BLF, the simulation atomistic model consisted of 640 unit cells (8×8×10) with 2896 ions, corresponding to the neutralized composition $La_{0.05}Ba_{0.95}FeO_{2.525}$. The cut off radius for the short-range force was set at 1.1 nm, while the long range Coulombic force was solved using Ewald summation method with an accuracy of 10^{-5} for the relative error of forces. In order to study the thermally activated diffusion, 5 distinct temperatures were computed, ranging from 1173 K to 1573 K with a step of 100 K. The simulation temperature is higher than intermediate temperature because the obtained diffusivity is more reliable. The oxygen vacancy sites and the La substitution sites were generated randomly in each atomistic model. 7 models with different vacancy and substitution sites were computed at each temperature to ensure the reliability of the simulation results, since the oxygen diffusivity can be significantly affected by the homogeneity of the dopant distribution.[50] The same strategy was applied to x = 0.1, 0.2 and 0.3 in $La_xBa_{1-x}FeO_{(x+5)/2}$ so as to study the effect of increasing the doping level. In the computation, periodic boundary conditions were imposed and the isothermal-isobaric (NPT) ensemble was used with the Nose-Hoover thermostat. The pressure was set to 1 atm for all the simulation. The integration of the governing equation was performed with the Verlet integrator at a time step of 1 fs. The system was first equilibrated at the set temperature for 100 ps and then a consecutive 400 ps run was performed for data collection. The fluctuations of MD simulations using this method are shown in Figure S1 in the supplementary information. Mean squared displacement (MSD) was computed from the ionic trajectories by the multiple time origin method, i.e., MSDs were first computed for the time period from 0 to 200 ps, 1 to 201 ps and so on, and then these MSDs were averaged to produce the final MSD. Afterwards, the oxygen self-diffusivity was obtained from the MSD by Einstein's relation:[51]

$$\mathrm{MSD}(t) = 6Dt + B \quad (3)$$

where D is the self-diffusion coefficient, t is the time and B is a constant capturing the intercept.

Experimental

The dense BLF target for pulsed laser deposition (PLD) was prepared using the method described in the previous work.[35] The BLF thin films were deposited on a 10 × 10 × 0.5 mm (001)-orientated 8 mol% yttria-stabilized zirconia (YSZ, space group Fm-3m, MTI) substrate. Before deposition, the PLD (Neocera JP-788) chamber pressure was first lowered to 9 × 10^{-6} mTorr, followed by pre-heating of the substrate at a rate of 10 °C min^{-1} to 700 °C. A samarium doped ceria (SDC) interlayer with a thickness of approximately 5 nm was first deposited, prior to depositing the BLF film. The deposition was performed using a Nd:YAG laser (Continuum Surelite SLIII-10) at a wavelength of λ=266 nm, 1 Hz repetition rate, and at an oxygen partial pressure of 160 mTorr with the laser beam fluence about ~3.5 Jcm^{-2}. The repetition rate was lowered to 1 Hz from previously reported 10 Hz, [35] in order to obtain single crystal films. After deposition, the sample was subsequently annealed at 700 °C for 45 minutes under an oxygen partial pressure of 200 Torr. Afterwards, the substrate was cooled to room temperature at a rate of 10 °C min^{-1}.

Thin film x-ray diffraction (XRD) techniques including symmetric $\omega - 2\theta$ scan (normal XRD), rocking curve (RC), x-ray reflectivity (XRR), ϕ scan (in-plane XRD), and reciprocal space mapping (RSM) were performed on a high resolution diffractometer (Empyrean PANalytical), using a Cu Kα radiation ($\lambda = 1.5406$Å , 40 kV, 40 mA) and the atomic model illustrations were generated using VESTA. [52] Phase structure identification was conducted by normal XRD, which recorded the XRD patterns at room temperature with 2θ ranging from 10° to 100° and at a scanning step of 0.0131°. The RC was scanned with a ω range of 4° and at a scanning step of 0.01°. The film thickness was obtained using XRR with 2θ ranging from 0 to 4°. The ϕ scan was performed with a range of 360° and a scanning step of 1°. The strain condition between the film and the substrate was studied by RSM. The fast RSM program was used, which incrementally changed the ω angle and at every ω value, a 2θ scan was performed. The range and scanning step for 2θ were respectively 3.334° and 0.0131°, and for ω were 3.5° and 0.05°. The surface morphology of the thin films was examined using atomic force microscopy (AFM, Nanoscope IIIa/Dimension 3100), which operated at tapping mode with a scan rate of 0.5 Hz and with 512 samples/lines. The composition of elements and Fe valence state of the samples were analyzed by X-ray photoelectron spectroscopy (XPS, PHI 5600) with Al monochromatic X-ray at 150 W. Depth profiling XPS was performed using Ar sputtering gun with a 2 kV voltage and a 3 mm × 3 mm raster area; the extractor current was 100 μA and at this condition the reference sputtering rate for SiO2 was 0.35 Å/s. The XPS scan was performed every 2 minutes during the sputtering until the C content was not detectable. The atomic concentration was determined by Ba4d, La3d, Fe2p, O1s and C1s electrons.

Electrochemical impedance spectroscopy (EIS)[53] was measured using VSP Bio-Logic electrochemical workstation. Symmetric cells, taking the form of BLF/SDC/YSZ/SDC/BLF, were used and silver paste was utilized as the current collectors. As previously shown, the silver paste has only a minor impact on the catalytic performance of the material.[35] The measurements were performed at temperature ranging from 550 to 700 °C and at an oxygen partial pressure from 0.1 to 1 atm. The frequency domain swept from 500 mHz up to 0.1MHz with an amplitude of 10 mV for the sinusoidal AC voltage.

Results and discussion

Computational results

In the computation, the structural optimization of BLF using the mean-field approach gives a pseudocubic lattice parameter of BLF to be 3.947 Å at room temperature, which is within 2% of the experimental value,[34] confirming the validity of the potential model. In order to study the reasons for stabilization, we start from the BF material, which mainly exists in the cubic phase (Pm-3m), $BaFeO_{2.5}$, and the monoclinic phase ($P12_1/c$), $Ba_2Fe_2O_5$. Studies regarding the monoclinic $Ba_2Fe_2O_5$ have been carried out by Zou et al,[54] where information such as the atomic positions was provided. For the monoclinic phase, besides two oxygen atoms located at the 2a Wyckoff positions, the other atoms all settle on the 4e positions. The primitive cells for the cubic and

monoclinic phase are shown in Fig.1.

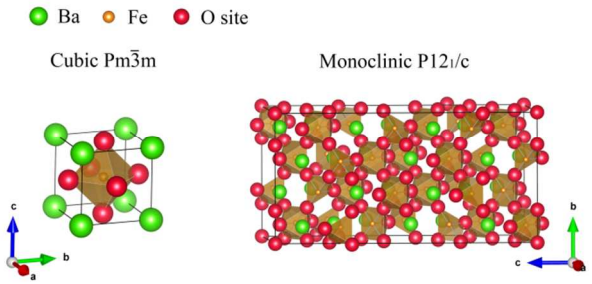

Fig. 1 Primitive unit cell illustrations of cubic phase with space group Pm-3m and monoclinic phase with space group P12$_1$/c.

The lattice energies per unit $BaFeO_{2.5}$ for the cubic and the monoclinic phase are computed to be -108.70 eV and -108.67 eV respectively. This small difference between the lattice energies hints that the two phases tend to coexist. After doping, a La^{3+} cation takes one site previously occupied by Ba^{2+}. This substitutional defect is denoted by $La_{Ba}^{\bullet}$, consistently with the Kröger-Vink notation.[55] The defect energies are calculated by the substitution reaction $La_{\infty}^{\bullet\bullet\bullet} + Ba_{Ba}^{x} = La_{Ba}^{\bullet} + Ba_{\infty}^{\bullet\bullet}$. The substitutional defects in the cubic phase and the monoclinic phase are -20.37 eV and -20.30 eV respectively. This defect energy difference indicates that upon doping with La^{3+}, the cubic phase has a lower energy than the monoclinic phase. This might be one of the determining factors that cause the phase transition of BF from monoclinic phase to the cubic phase. Note that the energy difference is small because it is computed by substituting only one Ba atom in the infinitely large sample. For a sensible fraction of doping, this single-atom defect energy difference would accumulate and eventually result in a large driving force for the transition. To further justify this conclusion, several more potential parameters[56-59] for the La^{3+}-O^{2-} pair are utilized, which yield the same conclusion. Interestingly, the same trend was also found for doping with elements such as Sm^{3+} and Gd^{3+} in the lanthanide group, and Y^{3+}.[44]

Tab. 1 Lattice and defect energies (eV) of the BF cubic phase and of the BF monoclinic phase.

	Cubic	Monoclinic	Potential reference
Lattice energy	-108.70	-108.67	42
Defect energy			
$La_{Ba}^{\bullet}$	-20.37	-20.30	43
	-21.29	-21.24	56
	-20.96	-20.84	57
	-20.12	-20.09	58
	-21.30	-21.27	59
$Gd_{Ba}^{\bullet}$	-24.16	-23.64	44
$Sm_{Ba}^{\bullet}$	-23.43	-23.03	44
$Y_{Ba}^{\bullet}$	-25.23	-24.59	44

The defect energies are summarized in Tab. 1. Considering that the higher valence state elements usually have a smaller ionic radius than Ba^{2+}, the conclusions we draw are consistent with those starting from the Goldschmidt tolerance factor. In addition, charge compensation is required after doping the Ba site with higher valence elements. Two primary mechanisms may exist: one by generating electrons and the other by filling the oxygen vacancies. The two respective reactions are shown below

$$La_2O_3 + 2Ba_{Ba}^{x} = 2La_{Ba}^{\bullet} + 2BaO + 2e' + \frac{1}{2}O_2 \quad (4)$$

$$La_2O_3 + 2Ba_{Ba}^{x} + V_O^{\bullet\bullet} = 2La_{Ba}^{\bullet} + 2BaO + O_O^{x} \quad (5)$$

To determine the dominant mechanism, the reaction energies need to be computed. This in turn requires the lattice energy for La_2O_3 and BaO. Their reaction energy difference, however, can be easily computed by subtracting (4) from (5) and then computing the following reaction

$$2e' + \frac{1}{2}O_2 + V_O^{\bullet\bullet} = O_O^{x} \quad (6)$$

Two major assumptions are made in order to compute the reaction energy of (6).[60, 61] First, the electrons are assumed to be small polarons, which locate on the Fe site, i.e., the electrons are essentially Fe^{2+}. This assumption implies that the material is not metallic, which is justified experimentally.[34] The energy of the polaron is calculated by first computing the energy of adding one electron to the Fe^{3+} and then subtracting the ionization potential of the Fe 3rd electron,[62] i.e., $E(e') = E(Fe^{2+}) - IP_3(Fe)$. Second, the oxygen dissociation follows several steps: the oxygen molecule dissociation, O atom reduced to O^- step and O^- reduced to O^{2-} step. The overall energy with oxygen reduction is therefore computed by $\Delta E_O = \frac{1}{2}D_e - EA_1 - EA_2 = 9.86$ eV, where D_e is the oxygen molecule dissociation energy, EA_1 and EA_2 are the first and second electron affinities.[57] The energy of filling an oxygen vacancy is denoted by $E(O)$, which is computed by the reaction $O_{\infty}'' + V_O^{\bullet\bullet} = O_O^{x}$. Again, all the defect energy calculations use the Mott-Littleton approach. The final reaction energy for (6) is computed by:

$$\Delta E = \Delta E_O - 2E(e') + E(O) \quad (7)$$

In the cubic phase, the result for (7) is -15.69 eV. The negative value hints that the filling of oxygen vacancies is the preferable charge compensation mechanism compared to generating electrons. Since the filling of oxygen vacancies is the primary charge compensation mechanism, it can be expected that this process is also associated with a decrease in the lattice energy because the Coulombic force becomes stronger when more ions, in this case oxygen anions, are introduced to the lattice. This, in addition, is another reason for the material stabilization after doping.

In the cubic phase, the filling of oxygen vacancies is found to be the predominant charge compensation mechanism, however, this reduces the concentration of oxygen vacancies. In addition, the substitutional defects, in this case the positively charged $La_{Ba}^{\bullet}$, are expected to be more tightly bound to the oxygen anions, potentially causing the moving oxygen anions to be trapped around the substitutional defect centre, resulting in a higher activation energy for the anion hopping. This binding strength can be quantified by the binding energy, a negative value of which stands for binding and a positive value for repulsion.[51] The binding energy between $La_{Ba}^{\bullet}$ and newly introduced oxygen anion at the nearest neighbor, O_O^{x}, is computed to be -0.75 eV, indicating a rather strong binding between them. It also indicates

that with the presence of La in the lattice, the oxygen vacancy formation tends to become less favorable due to the binding effect. The same situation is expected to happen on the surface of the material, which potentially results in a reduction of reaction rate with increasing La content, since the formation of oxygen vacancy at the surface becomes harder as well. In addition, the defect energy for oxygen vacancy, computed by $O_O^x = O_\infty'' + V_O^{\bullet\bullet}$, is 19.94 eV. This single point defect energy for oxygen vacancy is high, because of the empirical potential method we use here and its inability to calculate the atomic energy. However, the defect energy for the oxygen Frenkel pair is 1.29 eV per defect, which is a reasonable value. The defect energy for the defect dimer $(V_O^{\bullet\bullet}V_O^{\bullet\bullet})$ at the nearest neighbor is 43.62 eV, giving a binding energy of 3.74 eV. This value suggests that the oxygen vacancies tend to be separated. In the presence of $La_{Ba}^{\bullet}$ as the nearest neighbor, which forms a trimer defect cluster $(V_O^{\bullet\bullet}La_{Ba}^{\bullet}V_O^{\bullet\bullet})$, the binding energy further increases to 5.81 eV. The positive defect energy indicates that oxygen vacancy clustering is not likely to occur. In conclusion, a decreasing trend in the oxygen conductivity is expected with an increase in the doping level because of the decrease of oxygen vacancy concentration and the binding between $La_{Ba}^{\bullet}$ and the mobile oxygen anions. In oxygen permeation membrane experiments, a reduction in the oxygen permeation flux was observed when increasing the doping level of La.[37] The reason for the performance reduction might be connected to the decrease in oxygen conductivity with the increased doping level. It is further analyzed from MD, from which we could extract the oxygen diffusivity by fitting to Eq. (3). One typical MSD plot for BLF is shown in Fig. 2a, where the linear relationship between the MSD and time is found.

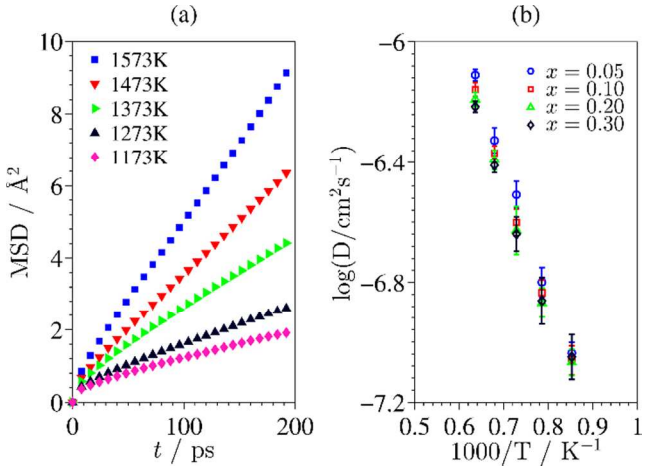

Fig. 2 (a) MSDs of oxygen anions evolution with time at various temperatures. (b) Oxygen self-diffusivity at different doping level. The error bars were obtained from 7 configurations at each condition.

The oxygen self-diffusivity as a result of changing the doping level is shown in Fig. 2b. The diffusivity results indicate that the increasing doping level has a negative effect on the oxygen conduction. The activation energies, obtained by fitting the Arrhenius equation of the self-diffusivity, are 0.85, 0.83, 0.81 and 0.77 eV for x = 0.05, 0.1, 0.2 and 0.3 respectively, which are consistent with previous measurements.[34] At a higher temperature, this phenomenon is more pronounced since the diffusion, an infrequent event, occurs more often with elevated temperature. In summary, the simulation results suggest that the cubic phase of BF can be stabilized by doping with La mainly due to the fact that the lattice energy of the cubic phase is reduced more than the monoclinic phase. Furthermore, the performance of La-doped BF is inversely related to the doping level, which is a result of reduced oxygen vacancy concentration and increased vacancy formation energy both in the bulk and on the surface. The computation results suggest that the doping level should be chosen so that the material starts to show a single phase when increasing the doping level. In light of these results, the experimental investigations were carried out on BLF.

Experimental results

The normal XRD pattern (background corrected), AFM surface morphology, the RC of BLF (001) plane and the XRR curve are shown in Fig. 3. The normal XRD, see Fig. 3a, shows that for the SDC interlayer and the BLF thin film, only the planes parallel to (001) are detectable, indicating good orientation of the interlayer and the film, with the (001) planes parallel to the (001) plane of the substrate YSZ. The normal XRD pattern signifies that single crystal thin film is obtained. The pseudocubic lattice parameter of BLF was computed to be 4.013 Å, which is slightly greater than that of the bulk value 4.0035Å.[34] In the latter context, a_{pc} is used to represent the pseudocubic lattice parameter. The dilation of thin film lattice was commonly observed in the PLD deposition[63, 64] and may be explained by different oxygen nonstoichiometry from the bulk, lattice mismatch between the film and the substrate and the film microstructure. In addition, the pseudocubic lattice parameters for SDC and YSZ are a_{pc}(SDC)=5.426 Å and a_{pc}(YSZ)=5.146 Å, respectively. The AFM surface morphology image of a 2 μm × 2 μm surface area is shown in Fig. 3b. It suggests that the surface of BLF thin film is of good quality, which has a root-mean-squared (RMS) surface roughness of 0.683 nm. The small surface roughness indicates that the effective surface area is close to the nominal area.

The RC was measured in order to assess the crystalline quality. A typical RC pattern is presented in Fig. 3c. The full width at half maxima (FWHM) of BLF (001) is approximately 0.903°, a value comparable to those films grown on YSZ substrates with doped ceria interlayer.[63] The relatively large FWHM could be attributed

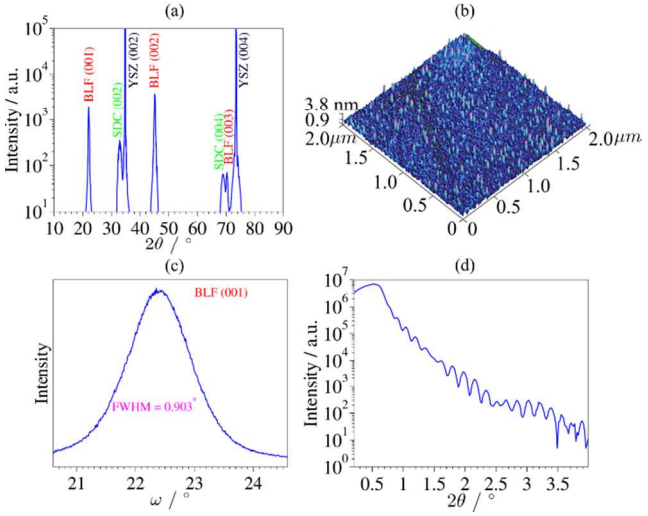

Fig. 3 (a) Normal XRD pattern, (b) AFM surface image, (c) Rocking curve and (d) XRR pattern of BLF thin films deposited on SDC-buffered YSZ (001) substrates.

to the non-uniform strain that is brought by the large lattice mismatch between the film and the interlayer, and the dislocation density.[65] The film thickness was measured using XRR. As shown in Fig. 3d, a thickness value of approximately 49 nm was detected, giving the growth rate of approximately 0.1 Å/shot.

We further investigated the in-plane film growth orientation by performing the in-plane XRD, as shown in Fig. 4. Four-fold in-plane symmetry was identified for the film BLF, the interlayer SDC and the substrate YSZ. The scan also revealed that the cubic lattice of the BLF thin film rotated 45° around the [001] direction, as schematically shown on the right-hand side of Fig. 4. This might be explained by the minimization of misfit energy between the substrate and the deposited films, since a_{pc}(SDC) is closer to $\sqrt{2}a_{pc}$(BLF) than a_{pc}(BLF).

The strain condition between the BLF film and the substrate YSZ was investigated by RSM. The scattering vector parallel and perpendicular to the crystal surface are expressed as

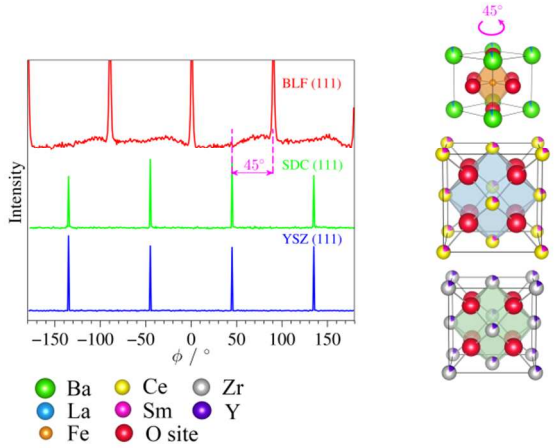

Fig. 4 In-plane XRD pattern showing a BLF thin film rotation 45° with respect to the substrate (YSZ) and the buffer layer (SDC), and schematic depiction of the crystal structure.

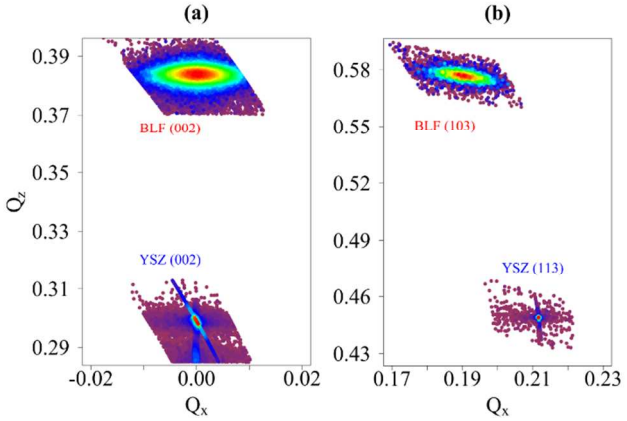

Fig. 5 Reciprocal space maps of (a) BLF (002) plane with YSZ (002) plane and (b) BLF (103) plane with YSZ (113) plane.

$q_x = 2\pi(cos(2\theta - \Omega) - cos(\Omega))/\lambda$ and $q_z = 2\pi(sin(2\theta - \Omega) + sin(\Omega))/\lambda$, respectively. Herein, we plot the reciprocal maps against normalized reciprocal space vectors with the in-plane vector $Q_x = sin(\theta)sin(\Omega - \theta)$ and out-of-plane vector $Q_z = sin(\theta)cos(\Omega - \theta)$, as shown in Fig. 5. It is further suggested in Fig. 5a, the map of symmetric planes (002), that the film is well oriented with the substrate, i.e., $[001]_{BLF}//[001]_{YSZ}$. Both the in-plane and out-of-plane lattice parameters could be computed from the reciprocal space vector at the points corresponding to the planes. For BLF (002), since $Q_x = 0$ and $Q_z = 0.3839$, the out-of-plane lattice parameter is computed to be c = 4.013 Å, which is consistent with that determined by normal XRD. Similarly, the in-plane lattice parameter of BLF is found to be a = 4.043 Å, slightly greater than the out-of-plane lattice parameter. By assuming a biaxial strain condition for the deposited film, the fully relaxed lattice parameters, $\hat{a}$ for in-plane and $\hat{c}$ for out-of-plane direction, could be solved. Herein we assume the fully relaxed cell retains a cubic shape, i.e., $\hat{a} = \hat{c}$. The lattice parameter $\hat{a}$, according to the equation $\Delta c/\hat{c} = -2\nu\Delta a/(\hat{a}(1-\nu))$ and $\nu = 0.3$ from our MD uniaxial loading simulation results, is determined to be 4.027 Å (see supplementary information for the calculation details). The in-plane strain, according to $\varepsilon = (a - \hat{a})/\hat{a}$, is computed to be 0.4%. This strain is not high enough to cause an obvious impact on the film performance,[66-68] thus the strain effect is excluded from the discussion. As opposed to the substrate, the reciprocal space point of the BLF film shows scattering both vertically and horizontally. This can be attributed to the finite thickness effect of the sample, i.e., the lattice parameter of the c axis varies slightly in different layers, and the mosaicity caused by the mismatch. The relatively small scattering areas suggest that good crystalline quality films are obtained.

The chemical composition of the as-deposited films was analyzed using X-ray photoelectron spectroscopy (XPS). The survey spectrum in Fig. 6a shows the existence of Ba, La, Fe, O and the adventitious C (corrected to binding energy 284.8 eV). The elemental composition matches well with the target composition, where the small deviation may be caused by surface effects. Therefore, the compositional gradation was studied using the depth profiling XPS, as shown in the inset of Fig. 6a. Fe content gradation is demonstrated, since the B site elements, usually transition metals, are believed to be catalytical active.[69]

Deficiency of Fe at the surface is observed, but it affects only the region up to a few nanometers under the surface. Improvement is expected by resolving the Fe deficiency at the surface. Following the survey scan, a high-resolution scan around the Fe 2p core level spectral was performed, aimed at determining the valence state of Fe so as to calculate the oxygen nonstoichiometry.

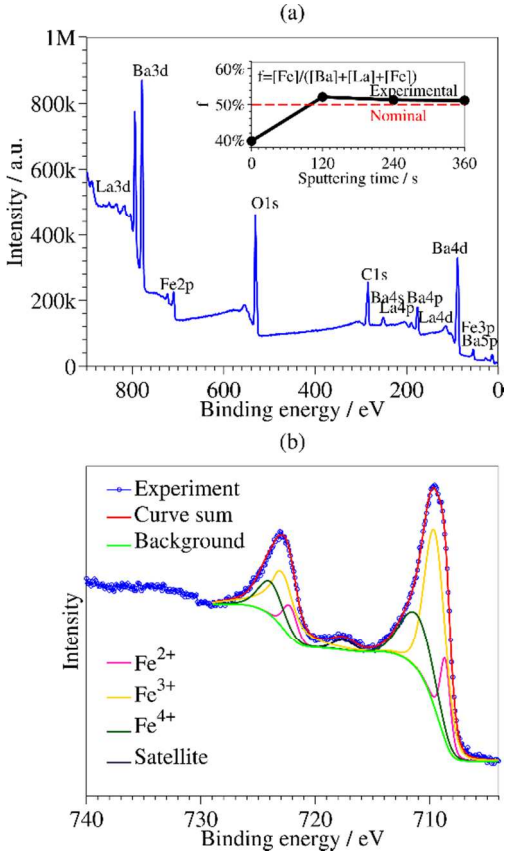

Fig. 6 XPS (a) survey scan at the surface and the atomic ratio change with sputtering time in the depth profiling XPS, and (b) high resolution scan around Fe 2p core level spectral at the surface.

In the fitting, the Shirley background subtraction method was used and the intensity of Fe $2p_{3/2}$ was set twice that of the Fe $2p_{1/2}$. As shown in Fig. 6b, the spin-orbit splitting of Fe 2p electron spectral, Fe $2p_{3/2}$ at 709.6 eV and Fe $2p_{1/2}$ at 723.1 eV, was fitted using 3 valence states of Fe, Fe^{2+}, Fe^{3+} and Fe^{4+}, since no combinations of 2 valence states could give a good fit. By curve fitting of the two peaks, 13.75% Fe^{2+}, 59.25% Fe^{3+} and 27% Fe^{4+} are identified, giving rise to an average Fe valence of 3.13. Therefore, the oxygen nonstoichiometry δ is determined to be 0.41. This value is close to 0.395, as measured in powder samples by iodometric titration at room temperature[34] and 0.409, as measured in polycrystalline films by similar a method as in this work.[35] The large oxygen vacancy concentration is one prerequisite condition for achieving high oxygen conductivity and is also beneficial to ORR.

ORR of the BLF thin film was characterized by EIS. A typical Nyquist EIS plot of a symmetric cell, BLF/SDC/YSZ/SDC/BLF, at 700 °C is shown in Fig. 7. The impedance patterns for various temperatures show similar features, i.e., the arcs exhibit depressed features and decrease in size dramatically with increasing oxygen pressure, which indicates the oxygen exchange at the surface governs the ORR.[70]

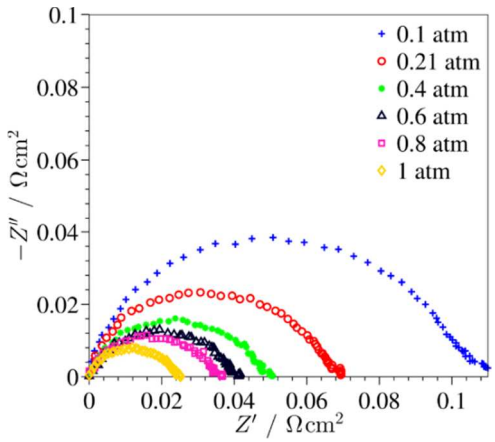

Fig. 7 Typical Nyquist EIS plots of a symmetric cell, BLF/SDC/YSZ/SDC/BLF, at 700 °C.

From the Nyquist plot, the polarization resistance R_p is defined as the length between the high frequency intercept and the low frequency intercept on the real axis. The surface oxygen exchange may follow a series of steps and it is suggested that the rate-limiting step can be determined by the dependence of polarization resistance on the oxygen partial pressure, specifically by fitting the exponential factor m in the relation $R_p \propto p_{O_2}^{-m}$.[71, 72] The case $m = 1$ corresponds to the rate limiting step of gas oxygen adsorption on the surface, i.e., $O_2(g) \leftrightharpoons O_2(ads)$, the case $m = 0.5$ corresponds to the chemical adsorption, which involves oxygen bond breaking, i.e., $O_2(ads) \leftrightharpoons 2O(ads)$, and the case $m = 0.25$ corresponds to the charge transfer process, $2O(ads) + 2e' + V_O^{\bullet\bullet} \leftrightharpoons 2O_O^x$. The change of R_p with respect to the oxygen pressures is shown in Fig. 8a. The fitted exponential factor $m = 0.55, 0.47, 0.46$ and 0.46 are derived at temperatures of 550, 600, 650 and 700 °C respectively, indicating that the dissociation of oxygen into adsorbed atoms is the predominant rate limiting step. In addition, the temperature dependence of the R_p is explored, as shown in Fig. 8b. The activation energy is determined using the exponential relation $1/R_p \propto \exp(-Ea/RT)$; the linear fitting lines and the corresponding activation energies are shown in the same figure.

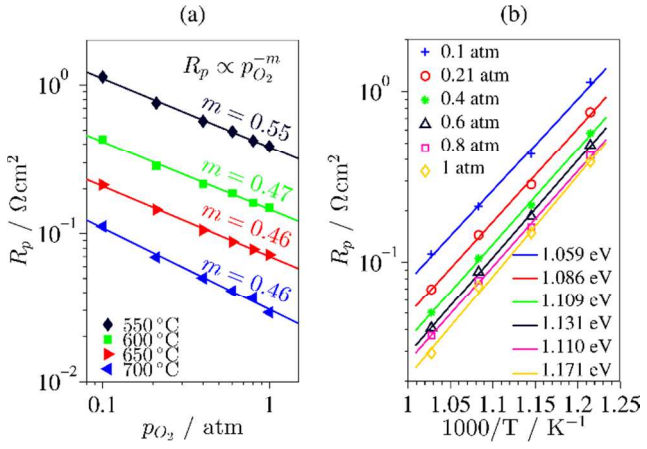

Fig. 8 (a) R_p dependence on oxygen partial pressure at various temperatures. The exponential factor m is fitted according to the relation captioned in the figure. (b) R_p dependence on temperature at different oxygen partial pressures, with corresponding activation energy Ea.

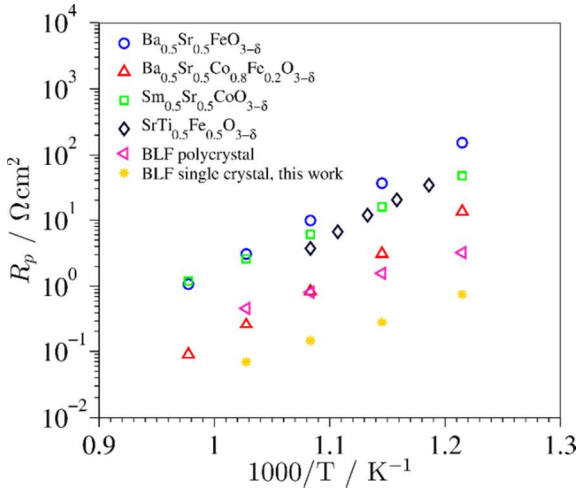

Fig. 9 R_p of BLF single crystal films compared to other thin film Fe-based materials and state-of-the-art Co-based materials at 700 °C and atmosphere oxygen pressure. The corresponding experimental data for $Ba_{0.5}Sr_{0.5}FeO_{3-\delta}$,[73] $Ba_{0.5}Sr_{0.5}Co_{0.8}Fe_{0.2}O_{3-\delta}$,[74] $Sm_{0.5}Sr_{0.5}CoO_{3-\delta}$,[75] $SrTi_{0.5}Fe_{0.5}O_{3-\delta}$[76] and BLF polycrystal[35] are taken from literature.

A decreasing trend of activation energy with decreasing oxygen partial pressure is observed, which might originate from the shortage of reactant supply at low oxygen content. It is expected that the increasing rate of the reaction speed with temperature in the low oxygen environment case is not as dramatic as the high oxygen content counterpart. The activation energies are, in general, smaller than those of the powder sample, but are greater than those of the polycrystalline sample. The trend is reversed for R_p, i.e., at the same temperature the powder sample exhibits the best performance, followed by the single crystalline sample and finally the polycrystalline sample.

The R_p values of several Co-based perovskite cathode materials and Fe-based materials, measured using dense thin films at ambient oxygen pressure, are shown in Fig. 9, together with the polycrystalline BLF and our current single crystal BLF film. The data show that the single crystal BLF film has the best performance with the smallest R_p.

Conclusion

High performance cathode material BLF was studied combining computational efforts and experiments on single crystal thin films. First, the stabilization reasons of BF upon doping with La were studied by lattice dynamics. It is concluded that with doping higher valence state element to the A site of the perovskite structure, the cubic phase can be stabilized with respect to the monoclinic phase. The atomistic simulations show that the reduction of the lattice energy in the cubic phase (Pm-3m) upon doping is greater than its counterpart in the monoclinic phase ($P12_1/c$). This results in an enhanced stability of the cubic phase in comparison to the monoclinic phase. The charge compensation mechanism upon doping with a high valence element is realized primarily by filling the oxygen vacancies, which further reduced the lattice energy and contributes to the material stabilization. The filling of oxygen vacancies and the introduction of a higher valence state element to the lattice, however, reduces the oxygen conductivity. This trend is confirmed by MD results.

Based on the simulation results, single crystal thin films of BLF were studied. High quality and relaxed films were obtained using PLD. The EIS measurement suggests that the single crystal film exhibited polarization resistance as low as 0.07 Ωcm^2 at 700 °C and ambient oxygen pressure, which is lower than the polycrystalline thin films and most Co-free materials. Moreover, this value is comparable to the state-of-the-art Co-based material.

Acknowledgments

The authors gratefully acknowledge HKUST for providing start-up funds, and the Research Grants Council of Hong Kong for support through the projects DAG12EG07-12, DAG12EG06, and ECS 639713.

Notes and references

[a] *Department of Mechanical and Aerospace Engineering, The Hong Kong University of Science and Technology, Hong Kong, SAR China. Tel: +852 2358 7187; E-mail: mefrank@ust.hk*
[b] *Department of Chemical and Biomolecular Engineering, The Hong Kong University of Science and Technology, Hong Kong, SAR China*
[c] *College of Energy, Nanjing University of Technology, No. 5 Xin Mofan Road, Nanjing 210009, PR China*
[d] *Department of Chemical Engineering, Curtin University, Perth, WA 6845, Australia*

1. A. B. Stambouli and E. Traversa, *Renew. Sust. Energ. Rev.*, 2002, 6, 433-455.
2. S. Singhal, *Solid State Ionics*, 2000, 135, 305-313.
3. A. J. Jacobson, *Chem. Mater.*, 2009, 22, 660-674.
4. S. B. Adler, *Chem. Rev.*, 2004, 104, 4791-4844.
5. D. J. Brett, A. Atkinson, N. P. Brandon and S. J. Skinner, *Chem. Soc. Rev.*, 2008, 37, 1568-1578.
6. D. Chen, G. Yang, Z. Shao and F. Ciucci, *Electrochem. Commun.*, 2013, 35, 131-134.
7. J. D. Nicholas, *Electrochem. Soc. Interface*, 2013, 49.
8. Z. Shao and S. M. Haile, *Nature*, 2004, 431, 170-173.
9. E. V. Tsipis and V. V. Kharton, *J. Solid State Electrochem.*, 2008, 12, 1367-1391.
10. J. Fleig, *Annu. Rev. Mater. Res.*, 2003, 33, 361-382.
11. F. S. Baumann, J. Fleig, H.-U. Habermeier and J. Maier, *Solid State Ionics*, 2006, 177, 1071-1081.
12. E. Perry Murray, M. Sever and S. Barnett, *Solid State Ionics*, 2002, 148, 27-34.
13. H. Tu, Y. Takeda, N. Imanishi and O. Yamamoto, *Solid State Ionics*, 1999, 117, 277-281.
14. S. P. Simner, M. D. Anderson, M. H. Engelhard and J. W. Stevenson, *Electrochem. Solid-State Lett.*, 2006, 9, A478-A481.
15. D. Chen, F. Wang and Z. Shao, *Int. J. Hydrogen Energy*, 2012, 37, 11946-11954.
16. C. Xia, W. Rauch, F. Chen and M. Liu, *Solid State Ionics*, 2002, 149, 11-19.
17. H. Tu, Y. Takeda, N. Imanishi and O. Yamamoto, *Solid State Ionics*, 1997, 100, 283-288.
18. F. Wang, D. Chen and Z. Shao, *J. Power Sources*, 2012, 216, 208-215.
19. C. Yang, Z. Yang, C. Jin, G. Xiao, F. Chen and M. Han, *Adv. Mater.*, 2012, 24, 1439-1443.
20. Z. Shao, S. M. Haile, J. Ahn, P. D. Ronney, Z. Zhan and S. A. Barnett, *Nature*, 2005, 435, 795-798.

21. D. Chen, C. Huang, R. Ran, H. J. Park, C. Kwak and Z. Shao, *Electrochem. Commun.*, 2011, 13, 197.
22. Z. Shao, W. Yang, Y. Cong, H. Dong, J. Tong and G. Xiong, *J. Membr. Sci.*, 2000, 172, 177-188.
23. H. Wang, Y. Cong and W. Yang, *Catal. Today*, 2003, 82, 157-166.
24. W. K. Hong and G. M. Choi, *J. Membr. Sci.*, 2010, 346, 353-360.
25. S. Švarcová, K. Wiik, J. Tolchard, H. J. Bouwmeester and T. Grande, *Solid State Ionics*, 2008, 178, 1787-1791.
26. C. Niedrig, S. Taufall, M. Burriel, W. Menesklou, S. F. Wagner, S. Baumann and E. Ivers-Tiffée, *Solid State Ionics*, 2011, 197, 25-31.
27. K. Efimov, T. Halfer, A. Kuhn, P. Heitjans, J. r. Caro and A. Feldhoff, *Chem. Mater.*, 2010, 22, 1540-1544.
28. H. Wang, C. Tablet, A. Feldhoff and J. Caro, *Adv. Mater.*, 2005, 17, 1785-1788.
29. B. Wei, Z. Lü, X. Huang, Z. Liu, J. Miao, N. Li and W. Su, *J. Am. Ceram. Soc.*, 2007, 90, 3364-3366.
30. Z. Tao, L. Bi, Z. Zhu and W. Liu, *J. Power Sources*, 2009, 194, 801-804.
31. Q. Liu, X. Dong, G. Xiao, F. Zhao and F. Chen, *Adv. Mater.*, 2010, 22, 5478-5482.
32. A. B. Muñoz-García, D. E. Bugaris, M. Pavone, J. P. Hodges, A. Huq, F. Chen, H.-C. zur Loye and E. A. Carter, *J. Am. Chem. Soc.*, 2012, 134, 6826-6833.
33. K. Watenabe, M. Yuasa, T. Kida, Y. Teraoka, N. Yamazoe and K. Shimanoe, *Adv. Mater.*, 2010, 22, 2367-2370.
34. F. Dong, D. Chen, Y. Chen, Q. Zhao and Z. Shao, *J. Mater. Chem.*, 2012, 22, 15071-15079.
35. D. Chen, C. Chen, F. Dong, Z. Shao and F. Ciucci, *J. Power Sources*, 2014, 250, 188-195.
36. C. Sun, R. Hui and J. Roller, *J. Solid State Electrochem.*, 2009, 14, 1125-1144.
37. T. Kida, D. Takauchi, K. Watanabe, M. Yuasa, K. Shimanoe, Y. Teraoka and N. Yamazoe, *J. Electrochem. Soc.*, 2009, 156, E187-E191.
38. R. t. Shannon and C. Prewitt, *Acta Crystall. B-stru.*, 1970, 26, 1046-1048.
39. Y. A. Mastrikov, M. M. Kuklja, E. A. Kotomin and J. Maier, *Energ. Environ. Sci.*, 2010, 3, 1544-1550.
40. A. Chroneos, B. Yildiz, A. Tarancón, D. Parfitt and J. A. Kilner, *Energ. Environ. Sci.*, 2011, 4, 2774-2789.
41. Y. Choi, D. S. Mebane, M. Lin and M. Liu, *Chem. Mater.*, 2007, 19, 1690-1699.
42. H. Shiiba, C. L. Bishop, M. J. Rushton, M. Nakayama, M. Nogami, J. A. Kilner and R. W. Grimes, *J. Mater. Chem. A*, 2013, 1, 10345-10352.
43. M. T. Buscaglia, V. Buscaglia, M. Viviani and P. Nanni, *J. Am. Ceram. Soc.*, 2001, 84, 376-384.
44. D. R. Ou, F. Ye and T. Mori, *Phys. Chem. Chem. Phys.*, 2011, 13, 9554-9560.
45. Y. Wang, A. Huq and W. Lai, *Solid State Ionics*, 2014, 255, 39-49.
46. J. D. Gale and A. L. Rohl, *Mol. Simul.*, 2003, 29, 291-341.
47. C. R. A. Catlow, *J. Chem. Soc. Farad. T. 2*, 1989, 85, 335-340.
48. N. Mott and M. Littleton, *T. Faraday. Soc.*, 1938, 34, 485-499.
49. S. Plimpton, *J. Comput. Phys.*, 1995, 117, 1-19.
50. M.-Y. Yoon, K.-J. Hwang, D.-S. Byeon, H.-J. Hwang and S.-M. Jeong, *J. Power Sources*, 2014, 248, 1085-1089.
51. M. S. Islam, *J. Mater. Chem.*, 2000, 10, 1027-1038.
52. K. Momma and F. Izumi, *J. Appl. Crystallogr.*, 2011, 44, 1272-1276.
53. W. Lai and S. M. Haile, *J. Am. Ceram. Soc.*, 2005, 88, 2979-2997.
54. X. D. Zou, S. Hovmoller, M. Parras, J. Gonzalez-Calbet, M. Vallet-Regi and J. Grenier, *Acta Crystallogr. Sect. A: Found. Crystallogr.*, 1993, 49, 27-35.
55. F. Kröger, H. Vink, F. Seitz and D. Turnbull, *Solid State Phys.* , 1956, 3, 307-435.
56. M. R. Levy, R. W. Grimes and K. E. Sickafus, *Philos. Mag.*, 2004, 84, 533-545.
57. R. A. De Souza, M. S. Islam and E. Ivers-Tiffée, *J. Mater. Chem.*, 1999, 9, 1621-1627.
58. E. Béchade, O. Masson, T. Iwata, I. Julien, K. Fukuda, P. Thomas and E. Champion, *Chem. Mater.*, 2009, 21, 2508-2517.
59. L. Minervini, M. O. Zacate and R. W. Grimes, *Solid State Ionics*, 1999, 116, 339-349.
60. M. Exner, H. Donnerberg, C. Catlow and O. Schirmer, *Phys. Rev. B*, 1995, 52, 3930.
61. M. S. Read, M. S. Islam, G. W. Watson, F. King and F. E. Hancock, *J. Mater. Chem.*, 2000, 10, 2298-2305.
62. National Bureau of Standards, *National Standard Reference Data Series No. 34*, 1970, 2.
63. S. J. Ahn, E. Crumlin, Y. Orikasa, M. D. Biegalski, H. M. Christen and Y. Shao-Horn, *Angew. Chem. Int. Ed.*, 2010, 49, 5344-5347.
64. G. Kim, S. Wang, A. Jacobson, Z. Yuan, W. Donner, C. Chen, L. Reimus, P. Brodersen and C. Mims, *Appl. Phys. Lett.*, 2006, 88, 024103.
65. H. Guo, J. Burgess, S. Street, A. Gupta, T. Calvarese and M. Subramanian, *Appl. Phys. Lett.*, 2006, 89, 022509.
66. A. Kushima and B. Yildiz, *J. Mater. Chem.*, 2010, 20, 4809-4819.
67. R. A. De Souza, A. Ramadan and S. Hörner, *Energ. Environ. Sci.*, 2012, 5, 5445-5453.
68. M. Rushton, A. Chroneos, S. Skinner, J. Kilner and R. Grimes, *Solid State Ionics*, 2012, 230, 37-42.
69. Z. Wang, R. Peng, W. Zhang, X. Wu, C. Xia and Y. Lu, *J. Mater. Chem. A*, 2013, 1, 12932-12940.
70. S. Adler, J. Lane and B. Steele, *J. Electrochem. Soc.*, 1996, 143, 3554-3564.
71. M. Escudero, A. Aguadero, J. Alonso and L. Daza, *J. Electroanal. Chem.*, 2007, 611, 107-116.
72. D. Chen, R. Ran and Z. Shao, *J. Power Sources*, 2010, 195, 4667-4675.
73. L. Wang, PhD Thesis, Max Planck Institute for Solid State Research, 2009.
74. F. Baumann, J. Fleig, H.-U. Habermeier and J. Maier, *Solid State Ionics*, 2006, 177, 3187-3191.
75. F. Baumann, J. Fleig, G. Cristiani, B. Stuhlhofer, H.-U. Habermeier and J. Maier, *J. Electrochem. Soc.*, 2007, 154, B931-B941.
76. W. Jung and H. L. Tuller, *J. Electrochem. Soc.*, 2008, 155, B1194-B1201.